

Supplement of

Complexation strength between organic carbon and transition metal ions dominates the photochemical conversion of SO₂ to sulfates

Shaojie Yang, Shiwei Lai, Jianwei Zheng, Hao Na, Fu Li, Wangjin Yang, Chong Han

School of Metallurgy, Northeastern University, Shenyang 110819, China

Correspondence to: Chong Han (hanch@smm.neu.edu.cn)

Contents	Pages
Section 1. Experimental section	S2–8
Section 2. Background experiment of SO ₂ uptake	S9
Section 3. Complexation evidences of OC with metal ions	S10–15
Section 4. Mechanism verification	S16–18
Section 5. Atmospheric implications	S19

Summary:

20 pages, including 17 figures, 10 texts and 3 tables.

Section 1. Experimental section

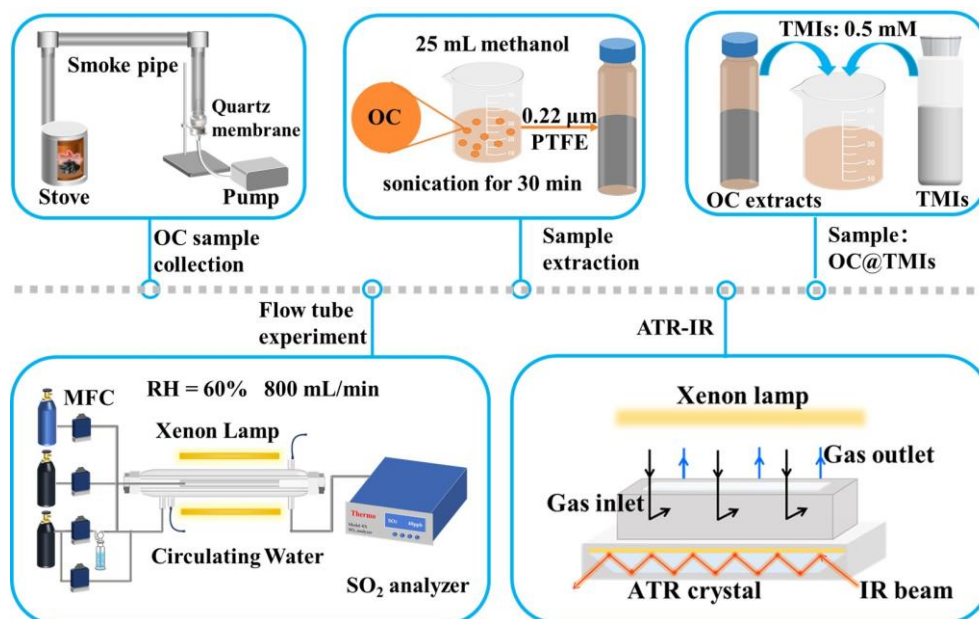


Figure S1. Diagram of OC samples preparation, flow tube reactor and in-situ attenuated total internal reflection infrared (ATR-IR) reaction cell.

Text S1: OC collection and preparation

The stove was commonly used in northern Chinese households and was acquired from the local market for the experiments. To address the ignition challenges of raw coal, solid alcohol and smokeless charcoal were initially employed to ignite approximately one-third of the coal sample (about 500 g). After successful ignition, the charcoal was removed and the remaining coal (around 1000 g) was added to sustain the combustion and generate smoke aerosols. The aerosols containing OC were collected onto quartz fiber filters (Whatman, $\text{Ø} = 90$ mm) positioned at the outlet of the flue. To ensure data reliability and repeatability, three separate sampling trials were conducted during the combustion. All quartz fiber filters were pre-baked at 450 °C for 6 h to remove the carbon pollutants. After sample collection, the filters were sealed in aluminum foil and preserved at -20 °C until OC extraction. A custom-designed hole punch (6 mm diameter) was used to cut circular sections from the filter. OC was extracted by the ultrasonication in methanol (25 mL, $\geq 99.7\%$) for 30 min, as shown in Fig. S1. The obtained extracts passed through a 0.22 μm polytetrafluoroethylene (PTFE) membrane filter, and then they were stored under refrigeration (2 °C) for subsequent analysis and experimental use.

Text S2: Chemicals

Sodium chloride (NaCl), Iron(III) chloride hexahydrate ($\text{FeCl}_3 \cdot 6\text{H}_2\text{O}$, $\geq 99.9\%$ metals basis), copper(II) chloride dihydrate ($\text{CuCl}_2 \cdot 2\text{H}_2\text{O}$, 99.99% metals basis), manganese(II) chloride tetrahydrate ($\text{MnCl}_2 \cdot 4\text{H}_2\text{O}$, 99.99% metals basis), zinc(II) chloride (ZnCl_2 , 99.95% metals basis), chromium(III) chloride hexahydrate ($\text{CrCl}_3 \cdot 6\text{H}_2\text{O}$, $\geq 99.9\%$ metals basis), cobalt(II) chloride hexahydrate ($\text{CoCl}_2 \cdot 6\text{H}_2\text{O}$, $\geq 99.9\%$ metals basis), magnesium(II) chloride hexahydrate ($\text{MgCl}_2 \cdot 6\text{H}_2\text{O}$, $\geq 99.9\%$ metals basis), nickel(II) chloride hexahydrate ($\text{NiCl}_2 \cdot 6\text{H}_2\text{O}$, $\geq 99.9\%$ metals basis) and aluminum(III) chloride (AlCl_3 , 99.99% metals basis) were purchased from Aladdin.

Text S3: Flow tube experiments

The reactor temperature was maintained at 298 ± 2 K by circulating water through the outer jacket. A relative humidity (RH) of 60% was obtained by regulating the ratio of humidified N_2 in the gas flow, and RH was recorded via a hygrometer (Center 314). Solar irradiation was simulated by two 250 W xenon lamps, and the corresponding spectral irradiance is presented in Fig. S2. The total irradiance in the wavelength range of 300-700 nm was determined to be 1.05×10^{16} photons $\text{cm}^{-2} \text{s}^{-1}$ with a spectroradiometer (ULS2048CL-EVO, Avantes). SO_2 was fed into the reactor via a movable injector, and a synthetic air flow (N_2/O_2 , 800 mL min^{-1} , SO_2 concentration of 40 ppb) was supplied to ensure laminar flow conditions. Control experiments confirmed that SO_2 loss was negligible under both dark and irradiation conditions in the blank reactor (Fig. S3).

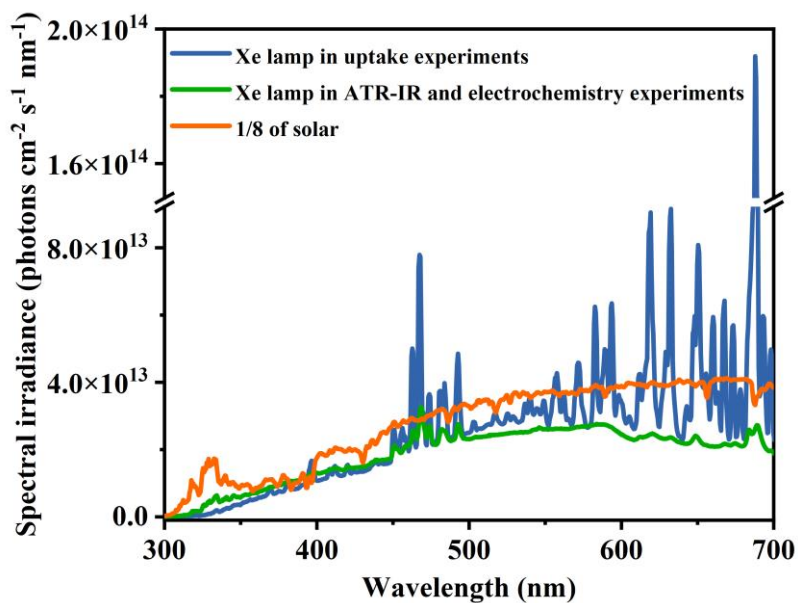


Figure S2. The spectral irradiance of xenon lamps and the solar spectrum measured for the 48° solar zenith clear sky at Shenyang (41.45 N, 123.25 E) on May 21st, 2024, at local time 12:00.

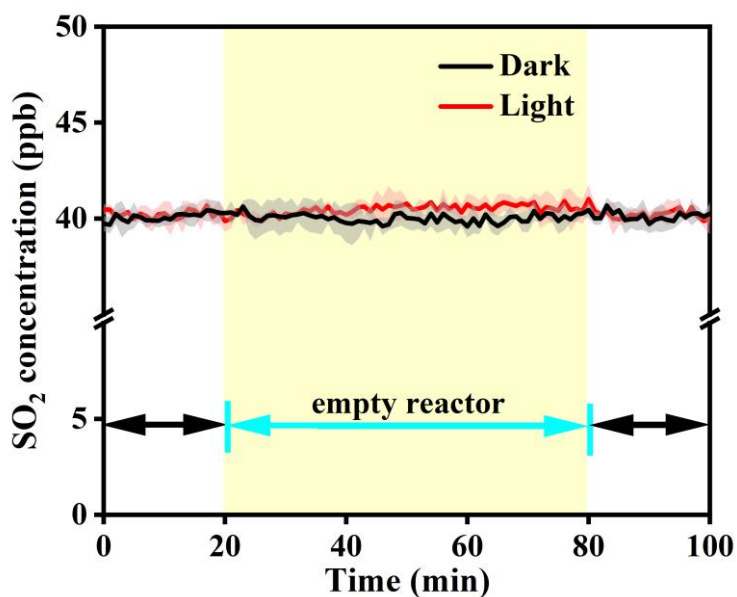


Figure S3. The uptake of SO₂ on empty reactor sample in the dark and under irradiation (1.05×10^{16} photons cm⁻² s⁻¹). All experiments were performed at 40 ppb SO₂, 298 K and 60% RH.

Text S4: Calculation of SO₂ uptake coefficient

The geometric uptake coefficients (γ) of SO₂ was calculated through the Eq. (S1),

$$\frac{\ln(C_0/C_t)}{t} = k_{\text{obs}} = \frac{\gamma v}{2r_{\text{tube}}} \quad (\text{S1})$$

where C_0 represents the initial SO₂ concentration (ppb); C_t means the SO₂ concentration (ppb) at a certain exposure time; t corresponds to the residence time (s) of SO₂ in the reactor. The observed first-order rate constant is expressed as k_{obs} (s⁻¹). The average molecular velocity (v) of SO₂ is 314 m s⁻¹, and the radius of the sample tube (r_{tube}) is 0.5 cm. The initial uptake coefficients (γ_i) was obtained from the maximum SO₂ uptake on OC within the first 1–2 min of the reaction, while the steady-state uptake coefficients (γ_{ss}) derived from stable SO₂ concentrations between 60 and 80 min.

Text S5: ATR-IR spectra

Samples (600 μL) were coated onto ZnSe plates and dried in an N₂ stream (100 mL min⁻¹) at room temperature. The samples were then purged with synthetic air (200 mL min⁻¹, N₂/O₂) at 298 K and 60% RH in the dark until the infrared spectrum stabilized. When samples were exposed to 2 ppm SO₂, the IR spectra were collected in the range of 4000–650 cm⁻¹ at 4 cm⁻¹ resolution for 100 scans, and the fresh samples were served as the background. A 500 W xenon lamp was used as the light source, with its irradiance shown in Fig. S2.

Text S6: Ion chromatography

To ensure the analyte concentration higher than the IC detection limit, the SO₂ concentration in the flow tube reactor was set at 200 ppb. Sulfates on the sample surface and gaseous H₂SO₄ at the reactor outlet were extracted with 5% formaldehyde aqueous solution (20 mL and 10 mL, respectively). All solutions were filtered through 0.22 μm PTFE membranes. During the IC analysis, a 13 mM KOH eluent was employed at 35 °C with a flow rate of 1 mL min⁻¹.

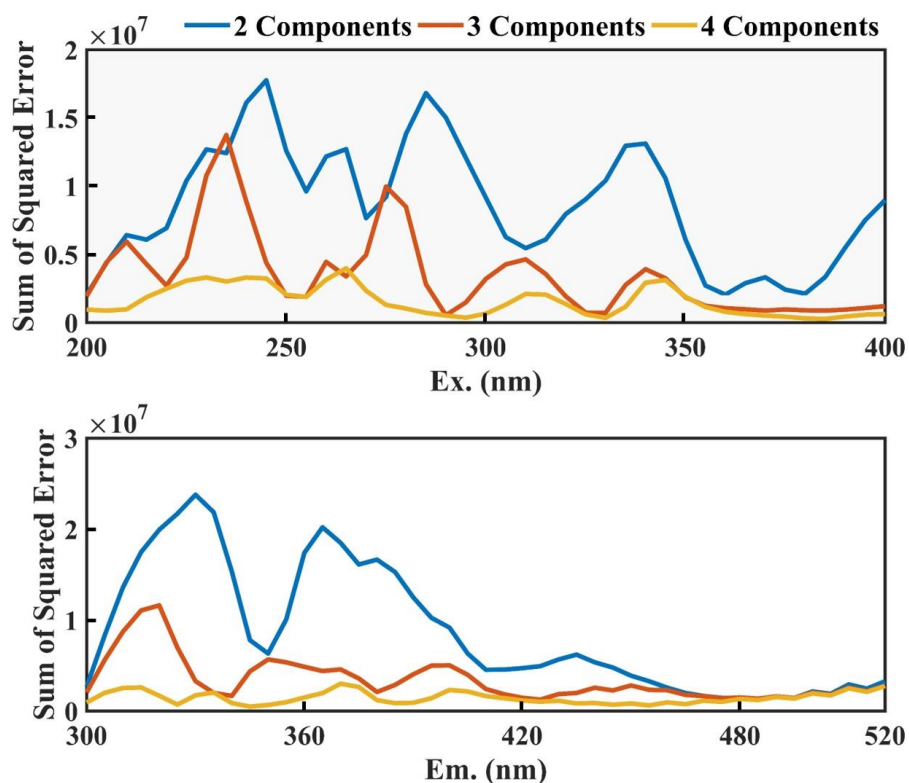


Figure S4. Sum of squared error plots showing the error as a function of Ex. and Em. wavelengths for varying component numbers in the spectral decomposition. The top panel presents the error for different numbers of components (2, 3, and 4 components) as a function of excitation wavelength (200–400 nm), while the bottom panel shows the error as a function of emission wavelength (300–520 nm). The blue, red, and yellow curves represent the sum of squared error for 2, 3, and 4 components, respectively.

Text S7: Electrochemical testing procedures

The three-electrode system comprised an Ag/AgCl reference electrode, a platinum counter electrode and a glassy carbon working electrode. 2, 2'-azino-bis (3-ethylbenzothiazoline-6-sulfonic acid) (ABTS) was selected as the reaction mediator for EDC. Initially, 35 mL phosphate buffer solution was added to the reaction cell and purged with nitrogen (N_2) for 10 minutes to eliminate atmospheric interference. The electrochemical workstation was operated in “Amperometric i-t curve parameters” mode at a redox potential (E_h) of +0.41 V. The xenon lamp was used to simulate solar irradiation, and its irradiance was shown in Fig. S2. Once the system stabilized, 0.5 mM ABTS solution was introduced as the redox mediator, followed by the addition of samples at 20-minute intervals in volumes of 1, 2, 3 and 4 mL, respectively.

Text S8: H₂O₂ testing procedure

After 1 h of irradiation, the reaction products deposited on the inner wall of the flow-tube reactor were rapidly extracted with 9 mL of methanol. 3 mL of the extract was subsequently mixed with 3 mL of a 5% v/v TiOSO₄ solution. The mixture was incubated in the dark for 15 min, and then the absorbance at 405 nm was recorded using a UV-vis spectrophotometer. To correct potential interference from the samples, the background test was conducted using parallel samples without the titanium reagent.

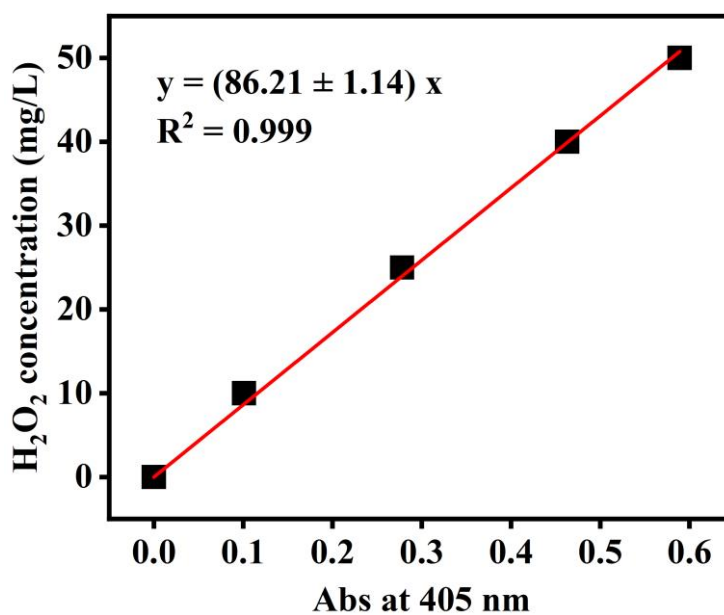


Figure S5. The standard curve of H₂O₂ obtained by using TiOSO₄ as an indicator.

Text S9: Energy calculations

The complexation energy (E_{complex}) between ligands and transition metal ions was calculated according to Eq. (S2),

$$E_{\text{complex}} = E_{\text{total complex}} - (E_{\text{L}} + E_{\text{M}}) \quad (\text{S2})$$

where $E_{\text{total complex}}$ is the total energy (kJ mol^{-1}) of the optimized metal–ligand complex; E_{L} and E_{M} are the energy (kJ mol^{-1}) of the isolated ligand and transition metal ions, respectively.

The adsorption energy (E_{ad}) for O_2 on the surfaces of the samples could be estimated by Eq. (S3),

$$E_{\text{ad}} = E_{\text{AB}} - (E_{\text{A}} + E_{\text{B}}) \quad (\text{S3})$$

where E_{AB} , E_{A} and E_{B} refer to the single-point energy (kJ mol^{-1}) of the adsorption complex, adsorbed O_2 and sample surface, respectively.

Section 2. Background experiment of SO₂ uptake

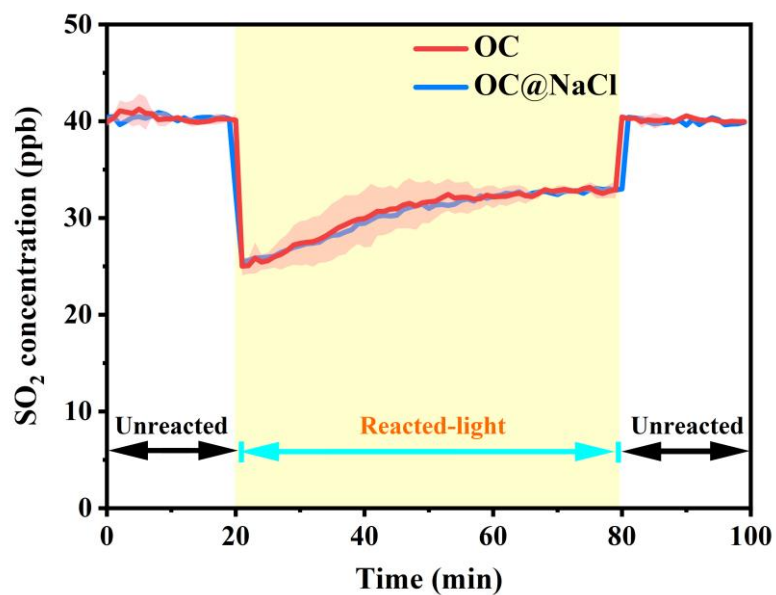


Figure S6. Temporal variation in the SO₂ concentration on OC (blue line) and OC@NaCl (red line) under irradiation. Reaction conditions: irradiance of 1.05×10^{16} photons $\text{cm}^{-2} \text{s}^{-1}$, 40 ppb SO₂, 298 K and 60% RH.

Section 3. Complexation evidences of OC with metal ions

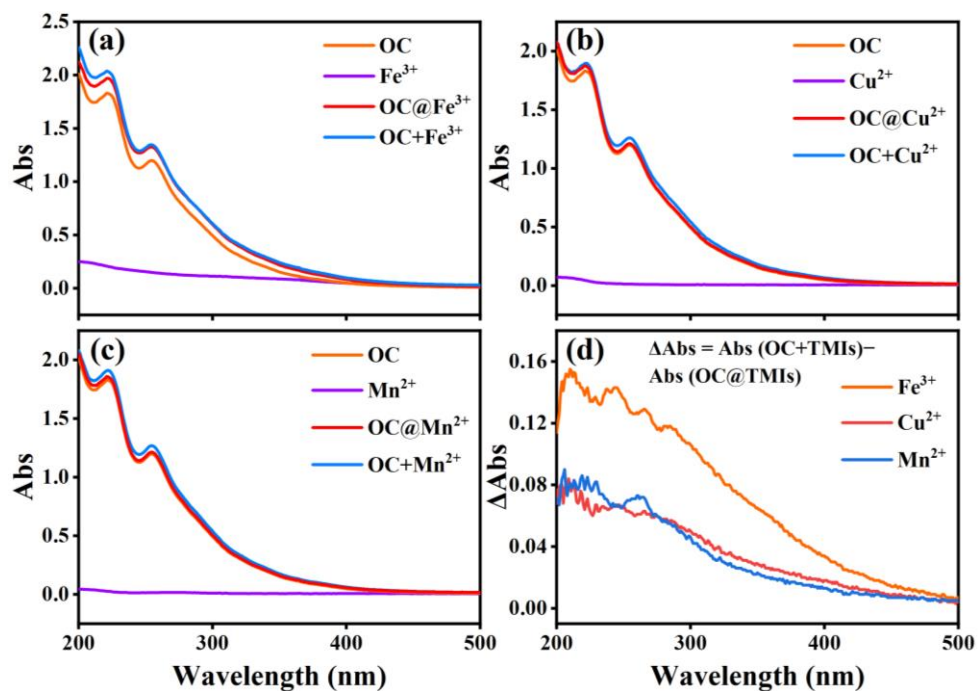


Figure S7. (a–c) The UV-Vis spectra of OC, FeCl₃, OC@Fe³⁺, OC+Fe³⁺, CuCl₂, OC@Cu²⁺, OC+Cu²⁺, MnCl₂, OC@Mn²⁺ and OC+Mn²⁺ (OC+TMIs was defined as the arithmetic sum of absorbance measured separately for OC and TMIs). (d) Differential absorbance spectra (ΔAbs) by subtracting the absorbance of OC@TMIs from that of OC+TMIs (Fe³⁺, Cu²⁺ and Mn²⁺).

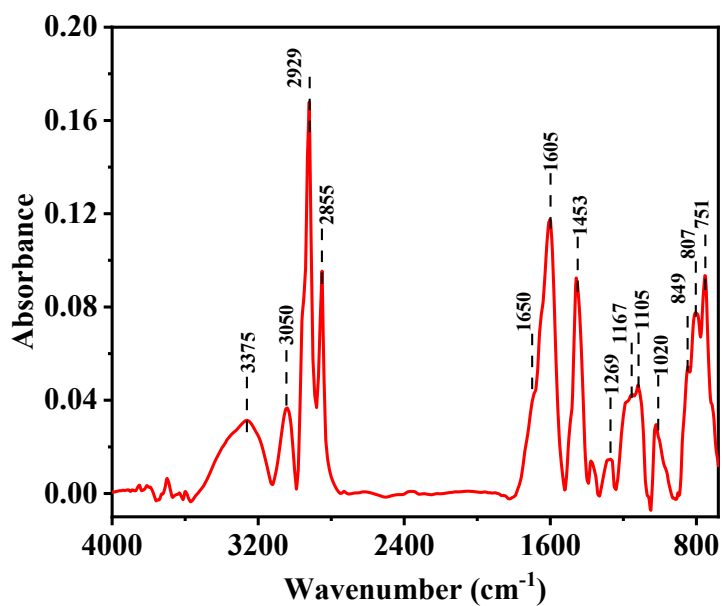


Figure S8. FT-IR spectra of OC.

Table S1. Assignments of functional groups in the FT-IR spectra of OC.

Wavenumber (cm ⁻¹)	Functional Groups
3375	Stretching vibration of O–H of carboxyl, phenol, and alcohol (Hay and Myneni, 2007)
3050	Stretching vibration of aromatic C–H (Sun et al., 2019)
2929	Asymmetric stretching vibration of C–H (Chen et al., 2016)
2855	Symmetric stretching vibration of C–H (Chen et al., 2016)
1650, 1605	Stretching vibration of aromatic C=O (Han et al., 2012)
1453	Asymmetric stretching vibration of methyl C–H (Sun et al., 2019)
1269, 1167	Stretching vibration of phenolic C–OH (Sun et al., 2019)
1105, 1020	Stretching vibration of C–O in ethers (Sun et al., 2019)
849, 807, 751	Out-of-plane bending vibration of aromatic C–H (Gaffney et al., 2015)

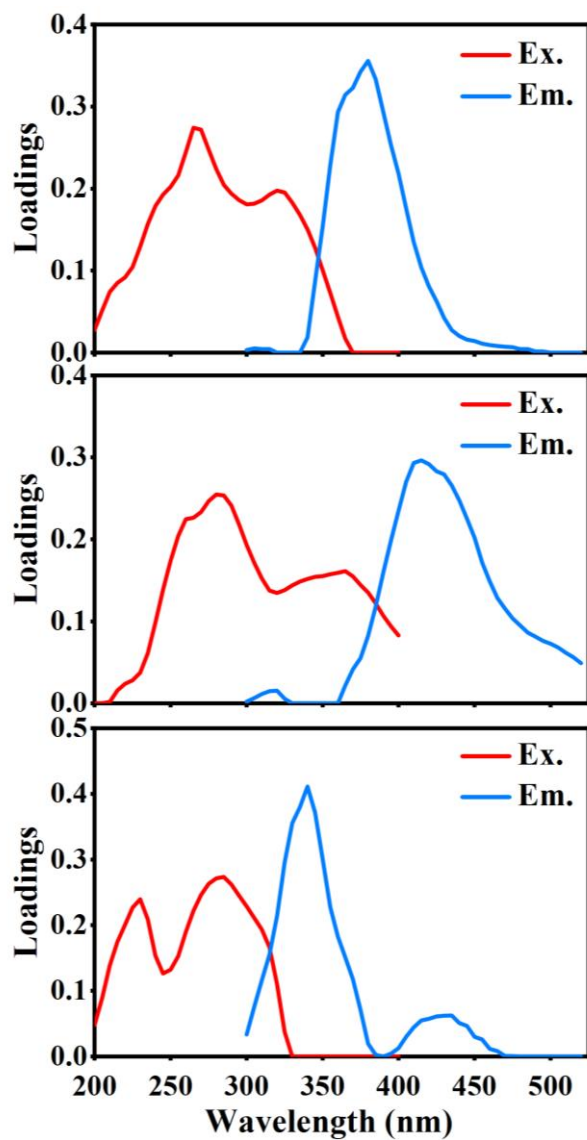


Figure S9. Three components extracted by PARAFAC.

Table S2. Peak position and possible components of different chromophores (C1–C3).

Composition	Ex. (nm)	Em. (nm)	Possible components
C1	265/320	380	Lowly oxidized OC
C2	285/370	420	Highly oxidized OC (oxygen-containing polar functional groups such as hydroxyl and carboxyl groups)
C1	200/260	340	Protein-like chromophores

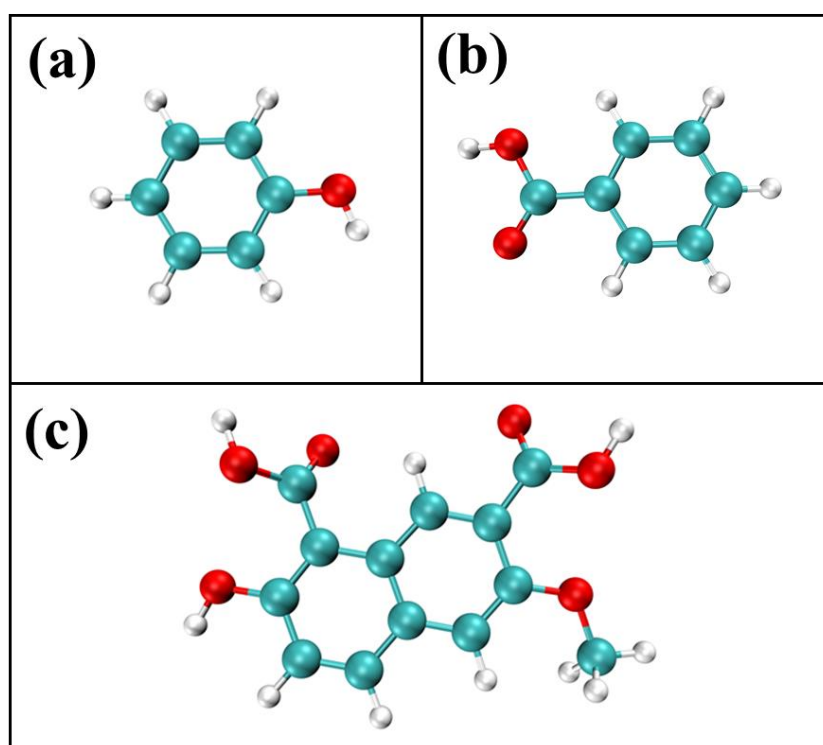


Figure S10. Configuration diagram of organic species: (a) phenol (PH), (b) benzoic acid (BA) and (c) model substance (MS). Oxygen atoms, carbon atoms and hydrogen atoms are shown in red, cyan and light gray, respectively.

Text S10: Complexation model construction

To better simulate real conditions in weakly acidic or aerosol environments, all ligands were modeled in their unprotonated (neutral) forms. The initial coordination model was constructed by positioning the molecules near the transition metal center, with donor atoms oriented toward the metal at an initial distance of ~ 2.0 Å. PH contained a hydroxyl ($-\text{OH}$) group, and its oxygen donated a lone pair for monodentate coordination. The carboxyl group ($-\text{COOH}$) within BA provided a carbonyl ($\text{C}=\text{O}$) and a hydroxyl ($\text{C}-\text{O}$) oxygen, enabling bidentate coordination and enhancing complex stability. In MS molecule, $-\text{OH}$ and $-\text{COOH}$ groups were placed adjacently, allowing for the formation of six-membered chelate rings upon metal binding. This chelation strengthened the coordination interaction but also improved environmental representativeness. Carbonyl oxygen ($\text{C}=\text{O}$) preferentially acted as the coordination site due to its higher electron density and favorable spatial orientation.

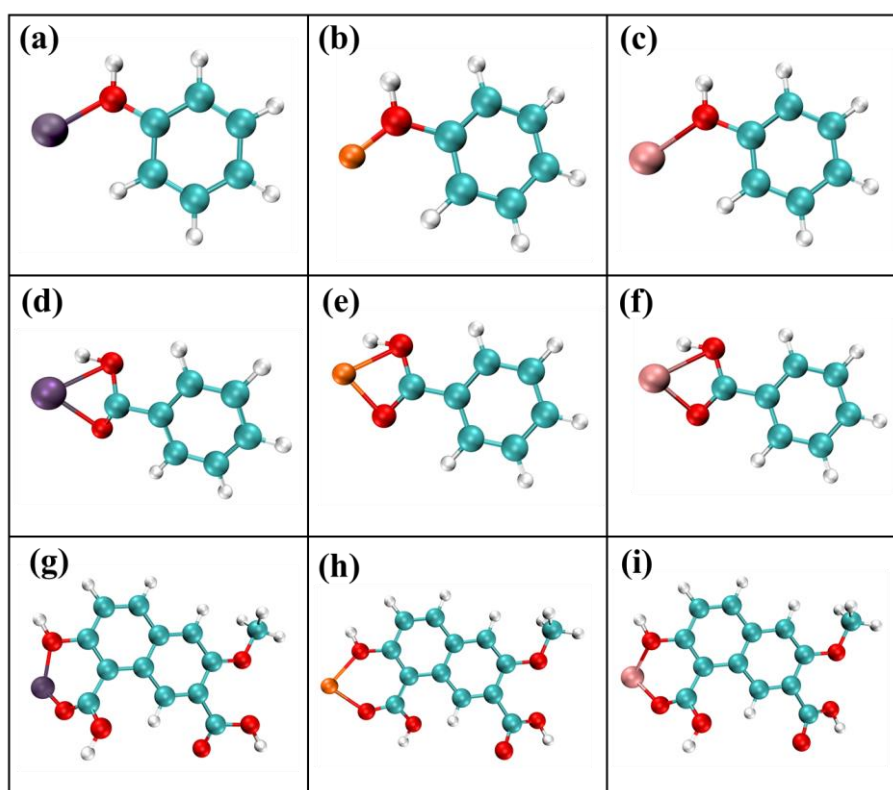


Figure S11. Configuration diagram of complexation model: (a–c) PH complexes, (d–f) BA complexes, (g–i) MS complexes. Oxygen atoms, carbon atoms, hydrogen atoms, iron atoms, copper atoms and manganese atom are shown in red, cyan, light gray, purple, orange and pink, respectively.

Table S3. Complexation energies of TMIs with BA, PH and MS.

Samples	Complexation energy (kJ mol ⁻¹)
PH@Fe ³⁺	-435.53
PH@Cu ²⁺	-102.42
PH@Mn ²⁺	-4.31
BA@Fe ³⁺	-505.01
BA@Cu ²⁺	-368.97
BA@Mn ²⁺	-295.53
MS@Fe ³⁺	-531.76
MS@Cu ²⁺	-107.29
MS@Mn ²⁺	-41.25

Section 4. Mechanism verification

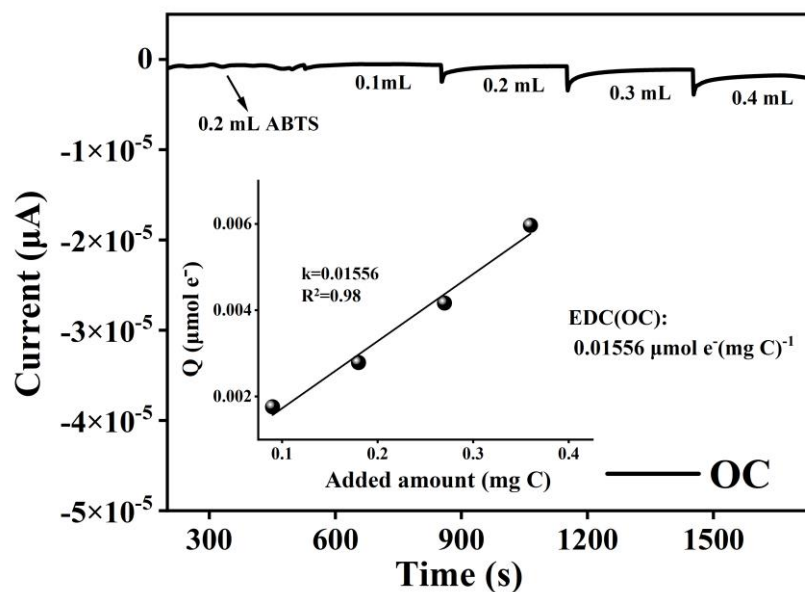


Figure S12. The oxidation current response in mediated electrochemical oxidation (MEO) and the electron donating capacities (EDC) of OC.

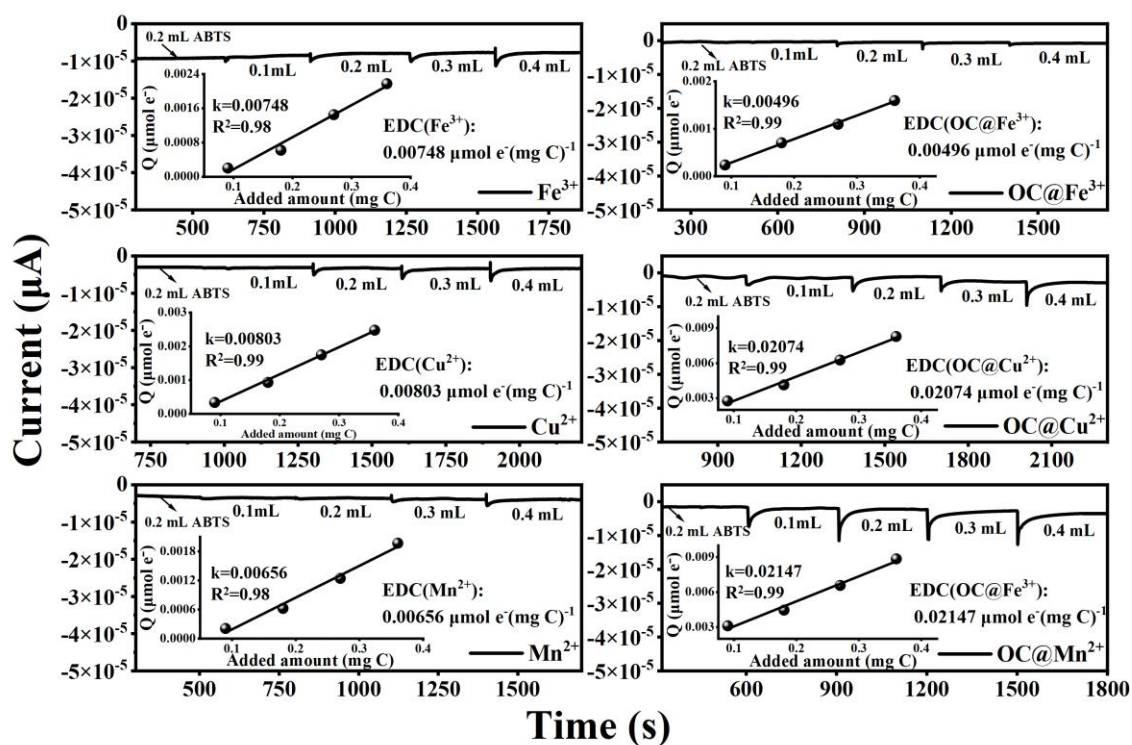


Figure S13. The oxidation current response in mediated electrochemical oxidation (MEO) and the electron donating capacities (EDC) of Fe^{3+} , OC@Fe^{3+} , Cu^{2+} , OC@Cu^{2+} , Mn^{2+} and OC@Mn^{2+} .

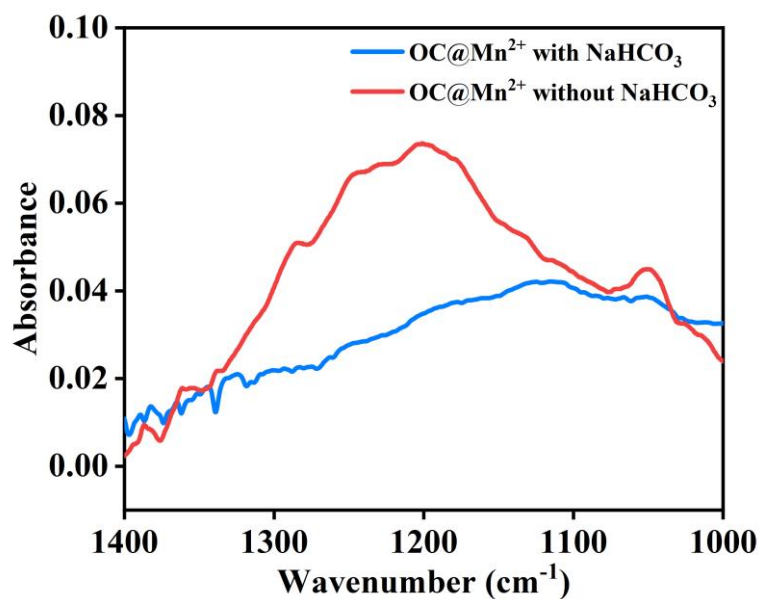


Figure S14. Sulfates formation on OC@Mn^{2+} with and without NaHCO_3 in the range of $1400\text{--}1000\text{ cm}^{-1}$ under irradiation ($7.40 \times 10^{15}\text{ photons cm}^{-2}\text{ s}^{-1}$). All experiments were performed at 2 ppm SO_2 , 298 K and $60\%\text{ RH}$.

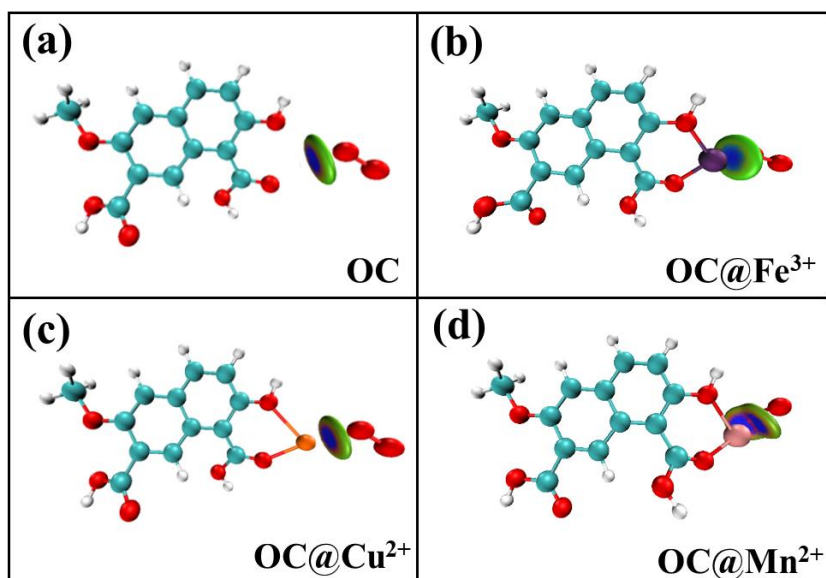


Figure S15. The IGMH diagram of the adsorption of O_2 on (a) MS, (b) MS@Fe^{3+} , (c) MS@Cu^{2+} and (d) MS@Mn^{2+} . The O_2 adsorption structure was established by placing the O_2 molecule approximately 2.0 \AA from the metal center, with its molecular axis aligned toward the coordination site.

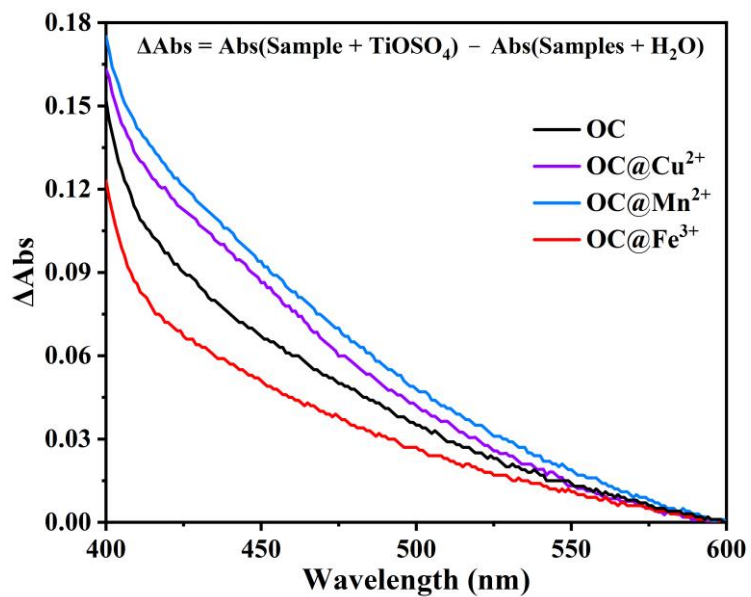


Figure S16. Differential absorbance spectra (ΔAbs) by subtracting the absorbance of samples+H₂O from that of samples+TiOSO₄ (OC, OC@Cu²⁺, OC@Mn²⁺ and OC@Fe³⁺).

Section 5. Atmospheric implications

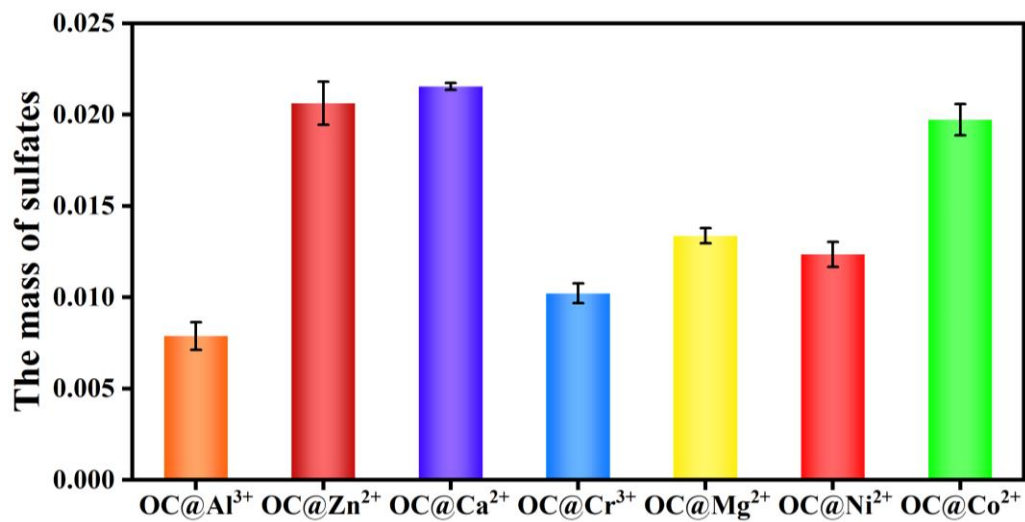


Figure S17. Mass of sulfates produced on OC@TMIs after the 10 h reaction with SO₂ under irradiation. Reaction conditions: irradiance of 1.05×10^{16} photons cm⁻² s⁻¹, 200 ppb SO₂, 298 K and 60% RH.

References

- Chen, Q., Ikemori, F., Higo, H., Asakawa, D., and Mochida, M.: Chemical structural characteristics of HULIS and other fractionated organic matter in urban aerosols: Results from mass spectral and FT-IR analysis, *Environ. Sci. Technol.*, 50, 1721–1730, <https://doi.org/10.1021/acs.est.5b05277>, 2016.
- Gaffney, J. S., Marley, N. A., and Smith, K. J.: Characterization of fine mode atmospheric aerosols by raman microscopy and diffuse reflectance FTIR, *J. Phys. Chem. A*, 119, 4524–4532, <https://doi.org/10.1021/jp510361s>, 2015.
- Han, C., Liu, Y., Ma, J., and He, H.: Key role of organic carbon in the sunlight-enhanced atmospheric aging of soot by O₂, *Proc. Natl. Acad. Sci. U.S.A.*, 109, 21250–21255, <https://doi.org/10.1073/pnas.1212690110>, 2012.
- Hay, M. B. and Myneni, S. C. B.: Structural environments of carboxyl groups in natural organic molecules from terrestrial systems. Part 1: Infrared spectroscopy, *Geochim. Cosmochim. Acta*, 71, 3518–3532, <https://doi.org/10.1016/j.gca.2007.03.038>, 2007.
- Sun, J., Shen, Z., Zhang, Y., Zhang, Q., Wang, F., Wang, T., Chang, X., Lei, Y., Xu, H., Cao, J., Zhang, N., Liu, S., and Li, X.: Effects of biomass briquetting and carbonization on PM_{2.5} emission from residential burning in Guanzhong Plain, China, *Fuel*, 244, 379–387, <https://doi.org/10.1016/j.fuel.2019.02.031>, 2019.